Revision 1

Magnetic anisotropy in natural amphibole crystals

Andrea R. Biedermann[1,a], Christian Bender Koch[2], Thomas Pettke[3] and Ann M. Hirt[1,*]

[1] Institute of Geophysics, ETH Zurich, Sonneggstrasse 5, 8092 Zurich, Switzerland; andrea.biedermann@ntnu.no, ann.hirt@erdw.ethz.ch

[a] Now at Department of Geology and Mineral Resources Engineering, Norwegian University of Science and Technology, Sem Sælands vei 1, 7491 Trondheim, Norway

[2] Department of Chemistry, University of Copenhagen, Universitetsparken 5, 2100 Copenhagen Ø, Denmark; cbk@chem.ku.dk

[3] Institute of Geological Sciences, University of Bern, Baltzerstrasse 1-3, 3012 Bern, Switzerland; pettke@geo.unibe.ch

Address for Correspondence: Prof. Dr. Ann M. Hirt, Institute of Geophysics, ETH Zurich, Sonneggstrasse 5, 8092 Zurich, Switzerland, phone: +41446332705, fax: +41446331065

Abstract

Anisotropy of magnetic susceptibility (AMS) is often used as a proxy for mineral fabric in deformed rocks. In order to do so quantitatively, it is necessary to quantify the intrinsic magnetic anisotropy of single crystals of rock-forming minerals. Amphiboles are common in mafic igneous and metamorphic rocks and often define rock texture due to their general prismatic crystal habits. Amphiboles may dominate the magnetic anisotropy in intermediate to felsic igneous rocks and in some metamorphic rock types, because they have a high Fe concentration and they can develop a strong crystallographic preferred orientation. In this study, the AMS is characterized in 28 single crystals and one crystal aggregate of compositionally diverse clino- and ortho-amphiboles. High-field methods were used to isolate the paramagnetic component of the anisotropy, which is unaffected by ferromagnetic inclusions that often occur in amphibole crystals. Laue imaging, laser ablation inductively coupled plasma mass spectrometry and Mössbauer spectroscopy were performed to relate the magnetic anisotropy to crystal structure and Fe concentration. The minimum susceptibility is parallel to the crystallographic a^*-axis and the maximum susceptibility is generally parallel to the crystallographic b-axis in tremolite, actinolite, and hornblende. Gedrite has its minimum susceptibility along the a-axis, and maximum susceptibility aligned with c. In richterite, however, the intermediate susceptibility is parallel to the b-axis and the minimum and maximum susceptibility directions are distributed in the a-c-plane. The degree of anisotropy, k', increases generally with Fe concentration, following a linear trend described by: $k' = 1.61\times10^{-9}$ Fe $- 1.17\times10^{-9}$ m^3/kg. Additionally, it may depend on the Fe^{2+}/Fe^{3+} ratio. For most samples, the degree of anisotropy increases by a factor of approximately 8 upon cooling from room temperature to 77 K. Ferroactinolite, one pargasite crystal and riebeckite show a larger increase, which is related to the onset of local ferromagnetic (*s.l.*) interactions below about 100 K. This comprehensive data set increases our understanding of the magnetic structure of amphiboles, and it is central to interpreting magnetic fabrics of rocks whose AMS is controlled by amphibole minerals.

Keywords: AMS (Anisotropy of magnetic susceptibility), magnetic properties, single crystal, amphibole, hornblende, actinolite, richterite, tremolite

1. Introduction

Members of the amphibole group are common rock forming minerals occurring in a wide range of igneous and metamorphic rocks. Amphiboles crystallize generally in idiomorphic, prismatic to needle-like habits; hence they often display preferential orientation in a deformed rock. This, combined with their intrinsic magnetic anisotropy, often makes amphiboles, together with phyllosilicates, the main carriers of magnetic anisotropy in igneous and metamorphic rocks. Amphiboles can be responsible for the magnetic fabric of a rock in two ways. Firstly, the amphibole minerals themselves can dominate the paramagnetic anisotropy (e.g. Borradaile et al. 1993; Schulmann and Ježek 2011; Zak et al. 2008). Secondly, the shape of magnetite inclusions can be controlled by the crystallographic preferred orientation (CPO) of amphiboles, which in turn is responsible for the magnetic anisotropy (Archanjo et al. 1994).

Because amphiboles possessing a CPO can be an important carrier of the magnetic anisotropy in a rock, it is essential to quantify their intrinsic anisotropy of magnetic susceptibility (AMS). Until now, only a few studies have been conducted on the AMS of amphibole single crystals, returning inconsistent results. Finke (1909) measured one hornblende crystal and found the maximum susceptibility at an angle of -21°55' to the crystallographic *c*-axis. Wagner et al. (1981) measured the magnetic anisotropy in six crystals from the hornblende group. In addition, they cited an unpublished study by Parry (1971), who examined high-field AMS in 18 hornblende crystals. Both studies concluded that the maximum principal susceptibility is sub-parallel to the crystallographic *c*-axis. However, in Wagner's hornblende, the minimum susceptibility aligns with the crystallographic *a*-axis, whereas it is parallel to *b* in Parry's study. This difference was attributed to the presence of ferromagnetic inclusions that influenced Wagner's low-field measurements (Wagner et al.

1981). Borradaile et al. (1987) measured five aggregates of amphibole crystals, including two actinolites and one sample each of hornblende, crocidolite (fibrous riebeckite) and glaucophane. Due to imperfect alignment of the individual grains within the aggregates, this study gives an estimate of the lower limit of the AMS. The authors provide no directional dependency. Lagroix and Borradaile (2000) measured two pargasite crystals and suggested that the maximum susceptibility is sub-parallel to the *b*-axis.

Differences in orientations of the principal axes of the AMS ellipsoid reported in these previous studies illustrate the importance of systematically investigating the magnetic anisotropy of amphiboles. In the present study, the intrinsic magnetic anisotropy of a series of amphiboles having a wide range of chemical compositions is characterized. The magnetic anisotropy was measured in low and high magnetic fields and at different temperatures in order to isolate the paramagnetic AMS. The paramagnetic AMS is then interpreted based on the general crystal structure of the amphiboles and their chemical composition. A main focus is put on the dependence of AMS on the Fe concentration.

2. Material and methods

Amphibole is an inosilicate that has the general formula $A_{0\text{-}1}B_2C_5T_8O_{22}(OH,F,Cl)_2$, where A = Na, K; B = Ca, Na, Fe^{2+}, Mn, Li, Mg; C = Mg, Fe^{2+}, Fe^{3+}, Al, Ti, Mn, (Ni, Cr, V, Li, Zn); and T = Si, Al. The main structural element defining amphiboles are $[(T_4O_{11})^{6-}]_n$ chains, i.e. double chains of tetrahedrally coordinated silica or aluminum. All tetrahedra of the same double chain point in the same direction, whereas two double chains with oppositely pointing tetrahedra are bonded by a band of octahedrally coordinated cations (C) (Figure 1). These cations occupy one of three sites (labeled M1, M2 and M3), which possess variable distortions of the octahedra, depending on the local environment. The M3 octahedra share 6 edges with adjacent octahedra, the M2 sites share 3 edges with octahedra and one with each of the two M4 polyhedra. M1 shares 5 edges with octahedra and 1 with the M4 polyhedron. The

sizes of the M1, M2 and M3 sites depend on the radius of the cation a given site hosts. Additionally, the sizes of M1 and M3 octahedra are also influenced by the amount of $(OH)^-$ substitution by F^- and Cl^-. The two tetrahedral double chains and the octahedral strip form so-called I-beams. Neighboring I-beams are bonded by cations in M4 (B) and A sites. The cations in the M4 sites have usually a higher than 6-fold coordination, and the coordination number is determined by the size of the cation. The A-site is coordinated by 12 surrounding oxygen atoms and can be vacant, partially occupied or filled.

Amphiboles are subdivided into 4 main groups, according to the main M4- or B-cation. Amphiboles that are classified as calcic (1), calcic-sodic (2) or sodic (3) have large cations, Ca and Na, in varying proportions, in the M4 sites. The M4 site in the Fe-Mg-Mn amphiboles (4) is occupied by smaller cations. Depending on the size of the cations in the M4 sites, the stacking sequence changes and thus amphiboles can possess a monoclinic or orthorhombic unit cell. Clinoamphiboles (space group *C*2/*m*) are more common than orthoamphiboles (*Pnma*). The symmetry elements as defined by the space groups can dictate the orientation of principal susceptibility directions according to Neumann's principle (Neumann 1885), which states that any physical property of a crystal has to include all symmetry elements of its space group. Therefore, each principal susceptibility has to be parallel to one of the crystallographic axes for the orthoamphiboles, while for clinoamphiboles one principal susceptibility has to be parallel to the crystallographic *b*-axis (Nye 1957).

With respect to the magnetic properties, it is the location and arrangement of Fe atoms that will be of greatest importance. This is due to the large magnetic moment of Fe in combination with a relatively high abundance in the crystal lattice. Iron can be present as Fe^{2+} or Fe^{3+}, whereby the Fe^{3+}/Fe^{2+} ratio rarely exceeds 1/2. Exceptions to this general rule can be found in Fe-rich hornblende (often referred to as oxy-hornblende) and hastingsite. In actinolite, Fe^{2+} prefers M1 and M3 over M2, and some Fe^{2+} can also be located at M4 (Deer et

al. 1997). Hornblende generally shows a similar Mg/Fe ratio in each of the M1, M2 and M3 sites, and Fe^{2+} can be located in M4. Fe^{3+}, like other small cations (e.g. Ti, Al), is preferentially located at the M2 sites (Deer et al. 1997). Metamorphic and skarn hornblende are different; in these minerals, Mg shows a preference for M2 and Fe has a tendency to be located in M1 or M3. In richterite, Fe^{2+} is enriched in the M2 sites compared to the M1 or M3 sites, where the Fe/Mg ratios are similar. If Mn is present, it occupies the M4 or M2 sites. In contrast, Fe^{2+} prefers M1 and M3 in riebeckite, where some Fe^{2+} can also enter M4. Fe^{3+} in riebeckite is located in M2 sites. In the anthophyllite-gedrite series, Fe^{2+} shows a preference for M4 over M1, M2 and M3, which possess similar Fe^{2+} concentrations. If there is a difference between M1, M2 and M3, the Fe^{2+} concentration is lowest in M2. When OH is substituted by F or Cl, this can also influence the site occupancy; Fe-F avoidance forces a larger proportion of Fe^{2+} into the M2 sites, whereas Cl prefers bonds to Fe^{2+} over bonds to Mg, which results in a preferential ordering of Fe^{2+} into the M1 and M3 sites (Deer et al. 1997).

2.1 Sample description

A collection of 28 natural single crystals and one aggregate was analyzed, chosen to cover a broad range of chemical compositions (Table 1). These include crystals from the calcic amphiboles (tremolite, actinolite and hornblende groups), sodic-calcic (richterite) and sodic (riebeckite) (clino-)amphiboles and one Fe-Mn-Mn orthoamphibole (gedrite). The individual crystals and the aggregate were cleaned with ethanol in an ultrasonic cleaner and oriented prior to measurements. Crystals were oriented based on Laue X-ray diffraction, performed at the Laboratory of Crystallography, ETH Zurich. Laue images were analyzed with the OrientExpress 3.4 crystal orientation software (Laugier and Filhol 1983). The oriented crystals were glued into diamagnetic plastic cylinders with no magnetic anisotropy. The crystallographic a^* (or a for the orthoamphibole), b and c directions corresponded to the

sample x, y and z-axes, respectively for magnetic measurements. The accuracy of crystal orientation is ± 5°. For the riebeckite aggregate, only the *c*-axis, which corresponds to the long axis of individual fibrous crystals, was oriented.

2.2 Chemical analysis

Bulk chemical composition was determined using laser ablation inductively coupled plasma mass spectrometry (LA-ICP-MS) at the Institute of Geological Sciences, University of Bern. Because most crystals could not be modified (e.g. for producing polished sections), the analyses were performed on crystal surfaces or cleavage planes, and for some crystals also on polished cross-sections (cf. Table A). LA-ICP-MS was preferred over electron probe microanalysis (EPMA) because LA-ICP-MS samples a bigger volume (here a cylinder of 90 µm diameter and about 60 µm depth). Hence minute impurities that may greatly affect the magnetic properties, such as exsolutions, melt or mineral inclusions, are also comprised in the mineral analysis. Notably metamorphic amphiboles often contain mineral inclusions, referred to as poikilitic growth. Per sample, four to six analyses were performed to obtain information on element homogeneity, expressed as one standard deviation (SD) in Table A (online supplementary).

The LA-ICP-MS used consists of a GeoLas Pro system coupled with an Elan DRC-e ICP-MS, optimized following procedures detailed in Pettke et al. (2012). SRM610 from NIST was used as the external standard material, with preferred values reported by Spandler et al. (2011). Data reduction employed SILLS (Guillong et al. 2008), and internal standardization was done by normalizing to 98 wt% total major oxides, thus allowing for 2 wt% of OH, F or Cl that cannot be measured with LA-ICP-MS. Data are considered to be accurate to better than 2 % 1 SD. The analytical accuracy is thus insufficient to reliably quantify Fe^{3+} and Fe^{2+} by LA-ICP-MS.

In order to determine the relative proportions of Fe^{2+} and Fe^{3+} and help in assigning the Fe to the various crystallographic sites Mössbauer spectra were measured on selected samples at the Department of Chemistry, University of Copenhagen. Absorbers were prepared by mixing powdered mineral samples and boron nitride into Perspex^R sample holders. Spectra were obtained at room temperature using a conventional constant acceleration spectrometer with the absorber perpendicular to the γ-ray direction and samples FAkt1 and FAkt4 were also measured at the magic angle (tilted at 54.7° relative to the γ-rays), to remove effects of mineral alignment in the powder. The spectrometer was calibrated using the spectrum of a thin foil of natural Fe at room temperature, and isomer shifts are given relative to the center of this absorber. All spectra exhibit three absorption lines which are interpreted as being composed of three overlapping doublets: one due to Fe^{3+} and two due to Fe^{2+}. The maximum intensities of the absorption lines were between 3% and 7% and baseline counts in the folded spectra were between 2 and 10 million counts. Lines were deconvoluted assuming Lorentzian lineshape and constraining the lines of each component to be identical. This constraint could not be applied to samples FAkt1 and FAkt4 due to preferred orientation of the grains in the powdered sample. New absorbers were prepared and measured using the magic angle and these spectra were suitable for the constraints (equal width and intensity of the two lines in the doublet). Assuming identical f-factors for each of the Fe components, the relative spectral areas were converted into abundances. The samples were scanned using amplitudes of 5 and 12 mm/s to achieve good spectral resolution of the amphibole components and to allow for checking for the presence of inclusions of magnetically ordered Fe oxides.

Site occupancies for individual cations were then determined based on the general formula $A_{0-1}B_2C_5T_8O_{22}(OH,F)_2$. Because the A site can be vacant or partially filled, the recalculation is not straightforward, unless the Fe^{2+}/Fe^{3+} ratio is known. For each sample, one of the following three models was used:

(1) When Mössbauer data were available, i.e., the Fe^{3+} and Fe^{2+} concentrations are known, the site distribution was defined based on a charge balance, setting the total number of cation charges to 46.

(2) For orthoamphiboles, it was assumed that no Na is located in M4. In this case, the number of cations minus Na and K equals 15.

(3) For clinoamphiboles, it was assumed that no Mg, Mn or Fe^{2+} occupy the M4 site and the total number of cations minus Ca, Na and K is equal to 13.

2.3 Magnetic measurements

Characterization of ferromagnetic inclusions. All magnetic measurements were made at the Laboratory for Natural Magnetism, ETH Zurich. Acquisition of isothermal remanent magnetization (IRM) was measured on selected samples in order to check for the presence of and identify ferromagnetic inclusions within the crystals. Samples were magnetized along the –z direction with an ASC Scientific IM-10-30 Pulse Magnetizer in a field of 2 T. Subsequently, the sample was remagnetized along the +z direction in increasing fields between 20 mT and 2 T. After each magnetization step, the IRM was measured on a 2G Enterprises, three-axis cryogenic magnetometer, Model 755.

Low-field AMS and mean mass susceptibility. Magnetic susceptibility can be described by a symmetric second-order tensor with eigenvalues $k_1 \geq k_2 \geq k_3$, or $|k_1| \geq |k_2| \geq |k_3|$ in the case of diamagnetic samples, i.e. k_1 corresponds to the most and k_3 to the least negative susceptibility for diamagnetic samples (Hrouda 2004). The corresponding eigenvectors define the directions of the principal susceptibilities. This can be represented by a magnitude ellipsoid of susceptibility, often referred to as anisotropy ellipsoid. The ellipticity can be described by the AMS degree $P = k_1/k_3$, or k' $= \sqrt{[(k_1 - k_{mean})^2 + (k_2 - k_{mean})^2 + (k_3 - k_{mean})^2]/3}$, where $k_{mean} = (k_1 + k_2 + k_3)/3$ and

AMS shape $U = (2k_2 - k_1 - k_3)/(k_1 - k_3)$ (Jelinek 1981, 1984). Low-field AMS was measured on an AGICO MFK1-FA susceptibility bridge. Measurements were performed at a frequency of 976 Hz and in a field of 200 A/m, or 500 A/m for samples with weak susceptibility. The low-field AMS was determined using a 15-position measurement scheme, in which every position was measured 10 times to increase the signal quality. This allows for an estimate of data quality, described by R_1, which is defined as the ratio between the deviation of the AMS ellipsoid from a sphere and noise level (cf. Biedermann et al. 2013). With the low-field method, the superposition of diamagnetic, paramagnetic and ferrimagnetic anisotropies are determined. The mean susceptibility was determined from the mass-normalized directional measurements and is referred to as mass susceptibility.

High-field AMS. High-field AMS was measured on a torque-meter (Bergmüller et al. 1994). Torque was measured while rotating the sample sequentially in three mutually orthogonal planes at 30° increments. Measurements were conducted in six different fields between 1.0 and 1.5 T and at two temperatures, room temperature (RT) and 77 K. For samples having weak torque signals, e.g. tremolite, the measurements were repeated in a more accurate mode and with 15° increments. The different temperature- and field-dependencies of diamagnetic, paramagnetic and ferrimagnetic contributions allow separation of the individual components of the high-field AMS (Martín-Hernández and Hirt 2001, 2004; Schmidt et al. 2007b). The method of defining the relative contributions and errors of the paramagnetic and ferromagnetic components to the AMS is described in Martín-Hernández and Hirt (2001). The paramagnetic susceptibility and its anisotropy increase with decreasing temperature. This increase can be quantified by the p_{77}-factor: $p'_{77} = k'(77\text{K})/k'(\text{RT})$.

Low-temperature magnetization curves. Susceptibility was measured as a function of temperature and crystallographic direction in three crystals. In addition, hysteresis loops were measured at several temperatures to check for the field-dependence of the susceptibility.

These measurements were made on a Quantum Design Magnetic Property Measurement System (MPMS) at the Laboratory for Solid State Physics, ETH Zurich. The crystals were cooled from room temperature to 2 K, during which the magnetization was measured every 10 K initially and in 1 K steps at low temperatures; temperature was stabilized before each measurement point. Measurements were made in a weak field of 10 mT to investigate if the crystals undergo magnetic ordering at low temperature. The same magnetization vs. temperature measurements were then repeated in a strong field of 1 T, to understand in detail the increase in the degree of anisotropy that is observed in the high-field AMS measurements at 77 K. At sufficiently high temperature, the susceptibility vs. temperature data could be fitted with a Curie-Weiss model for paramagnetic materials $\chi_{obs} = \mu_0 C/(T-\theta) = \mu_0\mu_B^2 g^2 S(S+1)N/(3k_b(T-\theta))$, where χ_{obs} is the molar susceptibility, $\mu_0 = 4\pi\times10^{-7}$ Vs/(Am) the permeability of free space, C the Curie constant, T the measurement temperature, θ the ordering temperature, μ_B is the Bohr magneton, g is Landé's g-factor, S is the spin number, N is the number of magnetic ions, and k_b is Boltzmann's constant. Ferrous Fe possesses a spin S = 2 and ferric Fe possesses a spin S of 5/2. Landé's g-factor and the ordering temperature θ depend on crystallographic direction and were determined based on the Curie-Weiss fits.

3. Results

3.1 Chemical composition

Bulk composition. Average chemical compositions of the samples and site occupancies are given in Tables A and B (online supplementary). For most crystals, the spot-to-spot variability is small, thus indicating homogeneous element distribution throughout the crystal and thus little growth zonation. Some crystals, however, show zonations of e.g. Al, K, Na or Fe. One sample, NMB535, was too big to fit the ablation chamber and could thus not be analyzed by LA-ICP-MS. A few samples, e.g. Amph1 or NMB44662, show too high T-site SiO_2 occupancies. For Amph1, where only EPMA data are available, we lack an explanation

for the apparent high SiO_2 concentration. The riebeckite sample, NMB44662, represents an aggregate of crystals that may contain melt or mineral inclusions or intercrystal minerals. The presence of such impurities is indicated by the considerably higher variability in major element concentrations when compared with the other amphibole analyses. The samples cover a range of chemical compositions, and the Fe concentrations vary between 0.03 and 25.5 wt% FeO. Other magnetic cations are present only in small amounts (0.01 – 1.1 wt% MnO, 5 – 1400 μg/g Cr, 0.8 – 920 μg/g Ni, and 0.01 – 65 μg/g Co) and thus have negliglible contributions to the overall magnetic properties.

Mössbauer spectroscopy. Mössbauer analysis shows that all analyzed samples contain three doublets, one of which can be assigned to Fe^{3+}, which we refer to as Component 1, and two to high-spin Fe^{2+}, which are referred to as Component 2 and 3 (Figure 2, Table 2). Peak assignment is not straightforward due to the chemical variation in amphiboles, which causes the Mössbauer spectra to vary considerably between mineral types (e.g. Hawthorne 1983). Component 1 has an isomer shift between 0.36 mm/s and 0.45 mm/s, a quadrupole splitting between 0.26 mm/s and 0.78 mm/s, and a line width between 0.22 mm/s and 0.60 mm/s. The line widths are much smaller for tremolite and actinolite, indicating one unique site M2 for Fe^{3+}, but larger for hornblende and richterite, which may arise if Fe^{3+} is distributed over M1, M2 and M3 sites or if there is substitution of OH^- by O^{2-}, causing changes in the local environment at the M2 site.

Component 2 has an isomer shift between 1.06 mm/s and 1.15 mm/s, a quadrupole splitting between 1.92 mm/s and 2.18 mm/s, and a line width between 0.41 mm/s and 0.47 mm/s. Component 3 has an isomer shift between 1.11 mm/s and 1.16 mm/s, a quadrupole splitting between 2.58 mm/s and 2.82 mm/s, and a line width between 0.29 mm/s and 0.34 mm/s. The large line widths of Component 2 could indicate that there are unresolved doublets from more than one site; alternatively, they may result from variations in the local

environment of a single site. Several studies have proposed different peak assignments, based on the observed variation in isomer shift and quadrupole splitting (Abdu and Hawthorne 2009; Hawthorne 1983; Oberti et al. 2007). In the present study, Component 2 is assigned to Fe^{2+} that occupies the M2 site, in accordance with Reusser (1987) who shows that the quadrupole splitting in M2 lies in-between that of M1/M3 and M4.

The Fe^{2+}/Fe^{3+} ratio is lowest in the hornblende samples, ranging from 1.0 to 1.8, and highest in the tremolite with a ratio of 6.5 (Table 2). The actinolites possess Fe^{2+}/Fe^{3+}-ratios of 2.8 and 3.3, and the three richterites have Fe^{2+}/Fe^{3+}-ratios between 2.1 and 2.7. It should be noted that no magnetically ordered components could be detected in the wide amplitude scans in any crystal, except for Amph3. The Mössbauer spectrum of Amph3 shows two sextets indicating a ferrimagnetic contribution from non-stoichiometric magnetite.

3.2 IRM acquisition

Acquisition of IRM shows that magnetization increases rapidly in low fields, which indicates that these crystals contain a low coercivity mineral, such as magnetite or its weathering product maghemite (Figure 3). The IRM of some crystals, e.g. Trem3, Hbl2 and FAkt1 is saturated by 200 mT, indicating that only a low coercivity phase is present. In other crystals, e.g. Trem2 and Akt1, saturation IRM is approached more slowly, which suggests that a high coercivity mineral such as hematite may also be present. The coercivity of remanence, which is affected by the type of ferromagnetic inclusions within the crystals, varies between 40 and 120 mT, whereby it is highest in Akt1 for which the IRM is not completely saturated. The amount of the high coercivity component is relatively small and should not influence the torque signal. The low coercivity component, however, is significant in some crystals and thus needs to be separated in order to obtain the paramagnetic anisotropy.

3.3 Mass susceptibility

316 Mass susceptibility, χ_m, was determined from the low-field anisotropy measurements,
317 and ranges from -3.5×10^{-8} m^3/kg to 2.6×10^{-6} m^3/kg. All tremolite and two of the richterite
318 crystals (FRi4, FRi5) are diamagnetic. In order to assess if ferromagnetic inclusions are
319 affecting the susceptibility of the remaining crystals, the measured values are compared with
320 the theoretical paramagnetic susceptibility that can be derived from the chemical composition.
321 According to Langevin theory, mass susceptibility can be given by $\chi_m = \mu_0 \frac{(L\mu_B)^2}{3RT}(\alpha {n_\alpha}^2 +$
322 $\beta {n_\beta}^2 + \cdots)$, where *L* is Avogadro's number, *R* is the gas constant, α, β... are the molar
323 amounts of the paramagnetic ions, and n_α, n_β... are the magnetic moments of the respective
324 ions given in terms of μ_B (Bleil and Petersen 1982). Manganese, Cr, Ni, and Co
325 concentrations are low in all samples, and only Fe is present in large enough quantities to
326 make a significant contribution to the mass susceptibility. Therefore, only Fe is used in the
327 theoretical calculation, which assumes the cations are in the divalent form, and that there is no
328 interaction between the magnetic moments of the cations.

329 Fifteen crystals show a good agreement between the measured and theoretical
330 paramagnetic susceptibility (Table 3). Crystals FAkt4, FAkt7, Amph, Amph3, Amph5, Hbl1
331 and Hbl2, however, show a significant difference that can be attributed to ferromagnetic
332 inclusions. Figure 4 shows the relationship between Fe concentration and mass susceptibility.
333 There is a good linear relationship for the group of crystals that do not contain a significant
334 amount of ferromagnetic inclusions, demonstrating that the mass susceptibility can be
335 quantitatively related to paramagnetic cations. The data can be fit by the relationship

336 $$\chi_m = (2.55 \times Fe - 2.30) \times 10^{-8} \text{ m}^3/\text{kg} \qquad \text{(Eq. 1)}$$

337 where *Fe* is the Fe concentration in wt%, assuming for simplicity that all Fe is Fe^{2+}. The
338 offset is close to the value of diamagnetic susceptibility of the tremolite crystals, and the fit is
339 in agreement with the theoretical increase of 2.30×10^{-8} m^3/kg per wt% FeO.

3.4 Low- and high-field magnetic anisotropy

The low- and high-field AMS are given in Tables 3 and 4. The diamagnetic and paramagnetic components extracted from high-field measurements can be attributed to the arrangement of cations in the silicate lattice, whereas the ferromagnetic component is related to Fe oxide inclusions or exsolutions. Figure 5 shows the directions of the principal susceptibilities of each mineral group for the low-field AMS and the dia-/paramagnetic part of the high-field AMS. The torque signal of most samples is dominated by the dia-/paramagnetic component. There is no systematic preference in the orientation of the ferromagnetic anisotropy for those samples with significant ferromagnetic content, indicating the presence of randomly oriented inclusions rather than exsolution features. The shape-factor (U) of the AMS ellipsoid is shown in Figure 6 as a function of degree of anisotropy, k'.

Tremolite group. The low-field AMS of tremolite is marginally significant, with R_1 between 0.4 and 2.2, and it cannot be excluded that the measured AMS directions are influenced by the holder signal (cf. Biedermann et al. 2013). The high-field AMS, despite the weak torque signal, shows some relationship to the crystallographic axes (Figure 5). Trem3 and Trem4 show similar directions with k_1 aligned along the crystallographic b-axis, but Trem1 has the k_2 axis and Trem2 k_3 along the b-axis. The degree of anisotropy (k') of the dia-/paramagnetic AMS is very small, ranging from 1.53×10^{-10} m^3/kg to 8.92×10^{-10} m^3/kg. The shape of the AMS ellipsoid is neutral, but oblate (Figure 6). The high-field torque signal is dominated by noise at 77 K. This deterioration in the torque response suggests that the diamagnetic susceptibility may be responsible for the observed AMS at room temperature, because the susceptibility becomes more isotropic with the enhancement of the paramagnetic susceptibility at 77 K.

Actinolite group. The Fe-concentration controls the susceptibility in the actinolite and ferroactinolite crystals. The principal directions of the low-field AMS have k_1 along the

crystallographic *b*-axis, k_2 along the crystallographic *c*-axis, and k_3 along the crystallographic *a**-axis, in all crystals except FAkt4 and FAkt7, which contain ferromagnetic inclusions (Figure 5). The principal axes become even better grouped for all crystals, when the paramagnetic AMS is isolated in high fields either at room temperature or at 77 K. Due to the lower Fe-concentration, *k'* is significantly lower in Akt1 compared to the ferroactinolites, which have *k'* around 3×10^{-8} m^3/kg (Figure 6). The shape of the AMS is oblate in all crystals, but slightly more oblate in Akt1, compared to the ferroactinolite, in which *U* is around 0.46. The factor p'_{77} is lowest in Akt1 with $p'_{77} = 7.75$, and between 9.47 and 11.15 for the ferroactinolite crystals.

Hornblende group. The orientation of the principal axes for the low-field AMS is scattered in relation to crystallographic axes in the crystals from the hornblende group, due to the significant ferromagnetic contribution to the susceptibility. The paramagnetic AMS, however, shows a similar orientation of its principal axes as found for actinolite, with k_1 parallel to the crystallographic *b*-axis, k_2 to the *c*-axis and k_3 to the *a**-axis in most samples (Figure 5). The same general relationship between eigenvectors and crystallographic axes is evident at 77K. For Amph3, the k_1 and k_2 axes are inverted at room temperature, but not at 77 K. It is interesting to note that the crystal with the lowest Fe-concentration, Amph1, shows the largest deviation of the k_2 and k_3 axes in the plane of the crystallographic *a*- and *c*-axes. The crystals in the hornblende group show the largest spread in *k'*, ranging from 2.39×10^{-9} m^3/kg to 1.66×10^{-8} m^3/kg, and *k'* generally increases with increasing Fe-concentration (Figure 7). The AMS ellipsoid is more oblate, compared to the ferroactinolite crystals, with *U* between 0.71 and 0.89. p'_{77} is between 7.29 and 8.97.

Richterite group. Although the richterite crystals all have a similar Fe concentration, their mass susceptibility is highly variable, and FRi4 and FRi5 are diamagnetic. The principal axes of the low-field AMS ellipsoid show almost no relationship to the crystallographic axes.

The dia-/paramagnetic component of the high-field AMS shows that the k_2 axes are generally along the crystallographic *b*-axis, and the k_1 and k_3 in the plane of the *a*- and *c*-axes. At 77 K, there is a better grouping of all three axes with k_1 and k_3 approximately 45° from the *c*-axis. The degree of anisotropy is very similar in all crystals, and is between 1.35×10^{-9} m^3/kg and 2.40×10^{-9} m^3/kg. The shape, however, is highly variable ranging from prolate to oblate. p'_{77} is between 5.25 and 9.86.

Riebeckite. The riebeckite sample is not a single crystal, but consists of an aggregate of fibrous grains, in which the fibers were all oriented along one direction. The maximum susceptibility is parallel to the long direction of the fibers. Because the magnetic anisotropy cannot be related to a single crystal, the orientations of the principal axes are not given. The principal susceptibilities provide a minimum estimate for the anisotropy, as the individual fibers may not be perfectly aligned within the aggregate. The sample shows the highest degree of anisotropy with $k' = 3.92\times10^{-8}$ m^3/kg, and a *U* of 0.71, which is comparable to the crystals from the actinolite and hornblende groups. The p'_{77}-factor is high with a value of 13.4.

Gedrite. The gedrite crystal has k_1 parallel to the crystallographic *c*-axis, k_2 parallel to the *b*-axis, and k_3 parallel to the *a*-axis both in low-field and high-field (Figure 5). The degree of anisotropy equals $k' = 2.08\times10^{-8}$ m^3/kg, the shape is weakly prolate with $U = -0.08$, and $p'_{77} = 8.12$.

3.5 Low-temperature magnetic properties

The inverse of the susceptibility is shown in as a function of temperature, crystal orientation and applied field in Figure 8. The paramagnetic susceptibility dominated the induced magnetization in the 1 T field, in which the ferromagnetic component is saturated. The susceptibility in actinolite FAkt5 follows an inverse linear relationship with temperature for T > ~100 K (Figure 8a). Below this temperature, local ferromagnetic ordering sets in when the applied field is along *b* or *c*, and local antiferromagnetic interactions occur when the

applied field is parallel to a^*. A Curie-Weiss fit to the paramagnetic range indicates paramagnetic Curie temperatures of -6 K, 21 K and 14 K in the a^*, b, and c directions, respectively. Landé's g-factor is between 2.4 and 2.5, indicating an orbital contribution to the magnetic moment. Both hornblende samples are strongly affected by ferromagnetic inclusions in the crystals, as seen from the non-linearity of the inverse susceptibility as a function of temperature (Figure 8b, c). A Verwey transition is observed in Amph3 (Verwey 1939; Walz 2002).

4. Discussion

4.1 Mass susceptibility and composition

Vernon (1961) demonstrated that the mass susceptibility of paramagnetic minerals correlates with the concentrations of Fe^{2+} and Mn, which agrees with our dataset when ferromagnetic inclusions in the crystals are negligible. Parks and Akhtar (1968) reported that the effective magnetic moment of Fe is strongly influenced by the crystal field, i.e. site symmetry, dimension or interatomic distance, and the type of bonding. They calculated an effective magnetic moment $n_{Fe2+} = 6.42$. The data presented here suggest a lower value of 5.5 to 5.6, a value that is in accordance with theoretical and experimental limits on the magnetic moment of Fe^{2+} (Parks and Akhtar 1968; Vernon 1961).

A linear relationship is observed between Fe concentration in the crystals and measured susceptibilities in the absence of ferromagnetic inclusions. Therefore, mass susceptibility can be used to deduce Fe-concentration, using the formula in Equation 1.

4.2 Low-field AMS and ferromagnetic inclusions

The principal directions of the AMS ellipsoid are more scattered for the low-field than for the high-field data. In samples whose low-field directions deviate from the paramagnetic high-field directions, the low-field directions plot close to those of the ferromagnetic

component. Even though present in minute concentrations, the ferromagnetic inclusions dominate both the mass susceptibility and its anisotropy. Since the ferromagnetic AMS does not show any systematic orientation of principal susceptibilities with respect to the amphibole crystal lattice, care has to be taken when interpreting low-field AMS, in particular in minerals in which magnetite inclusions are expected. Whether such inclusions occur in hornblende depends on the oxygen fugacity and on pressure. Magnetite is commonly found in shallow calcalkaline magmatic rocks. Therefore, care has to be taken to remove the magnetic signal due to these inclusions when interpreting magnetic fabrics in such rocks.

4.3 Relation between AMS, crystal structure and composition

Iron is not only expected to have a large influence on mass susceptibility, but also on the anisotropy of the susceptibility. In addition to concentration, the oxidation state and site distribution of Fe are important determining factors for the susceptibility anisotropy. Site distribution could have an effect in either of two ways: (1) different crystallographic sites have different distortions and local environments and therefore varying crystal fields, which may influence the ionic anisotropy of Fe, and (2) crystallographic sites are arranged along preferred axes or in planes, which defines the distances between nearest-neighbor Fe atoms in different directions and this affects interactions between individual magnetic moments.

Principal susceptibility directions. The principal axes of the AMS ellipsoids have similar orientations in actinolite and hornblende crystals (Figure 5). The only exception is Amph3, in which the k_1 and k_2 axes are interchanged at room temperature. The k_3 axis is parallel to a^* in all crystals, and this preference may result because a^* is normal to the plane of the octahedral bands. Iron is located in these bands; therefore, dipolar interactions will be smallest in the a^* direction. Another explanation can be found in crystal field theory. The amphibole M1 and M3 sites have similar crystal fields to the biotite M2 and M1 sites, respectively (Burns 1993). In biotite, this crystal field causes an easy-plane anisotropy with

464 the minimum susceptibility normal to the octahedral planes (Ballet and Coey 1982; Beausoleil
465 et al. 1983). A similar effect could occur in amphiboles. The k_1 axes are aligned along the
466 crystallographic *b*-axes, which can be explained by the fact that, within each octahedral band,
467 the distances between adjacent sites occupied by Fe is smallest in this direction. This effect
468 appears to outweigh effects caused by the orientation of the bands parallel to the *c*-axis.
469 Gedrite also has k_3 oriented along *a*, but in this case k_1 lies along the crystallographic *c*-axis,
470 and k_2 along the *b*-axis. This may be related to the different site preference of Fe^{2+}, which is
471 preferentially located in M1 - M3 in actinolite and hornblende vs. M4 in gedrite.

472 Richterite shows a grouping of k_2 about the crystallographic *b*-axis, and k_1 and k_3 are
473 distributed in the *a*-*c*-plane. At 77 K, the grouping of the k_2 axes along the *b*-axis becomes
474 stronger, and the k_1 and k_3 axes also show a grouping at an angle of approximately 45° from
475 the c-axis. At present it is not possible to explain why the principal axes show this preference.

476 The AMS of tremolite is very weak and does not show a consistent relationship with the
477 crystallographic axes when all samples are considered. Because the torque signal decreases
478 upon cooling, we surmise that paramagnetic and diamagnetic fabrics compete against one
479 another. For this reason, the magnetic anisotropy of this group will not be interpreted further.

480 **Anisotropy degree**. The paramagnetic anisotropy degree *k'* shows a linear increase
481 with Fe concentration (Figure 7). The actinolite crystals, however, display a slightly larger
482 degree of anisotropy than what would be expected from the trend defined by the other
483 samples. Actinolite has larger Fe^{2+}/Fe^{3+} ratios than hornblende or richterite. The fact that Fe^{3+}
484 behaves isotropically while Fe^{2+} possesses an easy-plane anisotropy in a distorted octahedral
485 crystal field (Beausoleil et al. 1983), could explain the relatively stronger anisotropy in the
486 Fe^{2+}-richer actinolite. However, there is no clear correlation between the Fe^{2+}/Fe^{3+} ratio and
487 the deviation of the anisotropy degree from the general trend. Furthermore, there is no

correlation between the ratio of the two Fe^{2+} components and deviation from the general trend.

The tremolite, hornblende, and richterite data follow a linear trend, where

$$k' = 1.61\times10^{-9}\times Fe - 1.17\times10^{-9}\ \mathrm{m^3/kg} \qquad \text{(Eq. 2)}$$

The fact that riebeckite exhibits the anisotropy degree predicted by this trend and its iron content, suggests that all fibers have similar orientations. Gedrite, on the other hand, has a lower anisotropy than expected. Possible explanations to this include differences in structure and symmetry (orthorhombic as compared to monoclinic in the other amphiboles), or the fact that Fe can be located in M4 sites in orthoamphiboles, whereas this site is occupied by larger cations in clinoamphiboles.

Temperature-dependence of the anisotropy degree. The degree of anisotropy increases by varying amounts with decreasing temperature. The factor p'_{77} is 7.8 for actinolite Akt1, between 7.3 and 8.3 for hornblende, between 7 and 9 for most richterite crystals and $p'_{77} = 8.1$ for gedrite (Figure 9). This is similar to p'_{77} in most minerals of the phyllosilicate group (Biedermann et al. 2014a), olivine (Biedermann et al. 2014b) as well as siderite (Schmidt et al. 2007a).

While no clear correlation appears between p'_{77} and Fe-concentration, those crystals with very low or high Fe concentration tend to have larger values of p'_{77} (Figure 9). This may be due to two effects. Firstly, when the diamagnetic contribution to the anisotropy is high due to very low Fe concentration, an increase in the paramagnetic susceptibility appears larger. Schmidt et al. (2007a) observed this effect in calcite. Secondly, the onset of local ferromagnetic coupling within the octahedral bands and local antiferromagnetic coupling normal to these bands at temperatures below about 100 K may also lead to a higher ratio, as found in biotite (Biedermann et al. 2014a). We may expect that these interactions can only

occur when Fe^{2+} cations are located sufficiently close to each other; hence, this effect is seen mainly in ferroactinolite with a high concentration of Fe^{2+} on the M1, M2 and M3 sites and in riebeckite, with the overall largest Fe concentration.

5. Implications

This new comprehensive data set on single crystals of amphibole minerals with variable composition and structure demonstrates that the intrinsic magnetic anisotropy is a function of both chemical composition and crystal lattice. The results presented here serve as an important basis for AMS studies in rocks whose AMS is dominated by amphiboles. The orientation of the principal AMS axes can be used as a proxy for rock texture. The degree of anisotropy in such rocks increases with (1) the strength of crystallographic preferred orientation of the amphiboles, and (2) the Fe concentration within the individual crystals. Thus, the AMS degree does not necessarily reflect the degree of deformation, but is related to Fe concentration. The AMS appears to be independent of site occupancy in clinoamphiboles, but the AMS degree increases with increasing percentage of M1, M2 and M3 sites that are occupied by Fe^{2+}, which might be used for a first-order estimate of Fe^{2+}/Fe^{3+} ratios.

The data presented in this study also highlight the influence of ferromagnetic inclusions, such as individual magnetite crystals. Their presence may dominate low-field AMS and override the anisotropy originating from the paramagnetic amphiboles. Consequently, a separation of paramagnetic and ferromagnetic contributions to the magnetic anisotropy is essential prior to determining amphibole CPO or interpreting rock texture based on magnetic fabric.

Acknowledgments: A. Puschnig, Natural History Museum Basel, A. Stucki, Siber+SiberAathal and P. Brack and S. Bosshard, ETH Zurich are thanked for providing

samples for this study. D. Logvinovich helped with the Laue method for crystal orientation. We are grateful to E. Reusser for assistance with recalculation of the mineral formulae. W.E.A. Lorenz kindly provided support with low-temperature measurements and data analysis. We thank W. Lowrie for his constructive comments. Mike Jackson and Jeff Gee are thanked for their thorough reviews. This study was funded by the Swiss National Science Foundation, projects200021_129806 and 200020_143438.

References

Abdu, Y.A., and Hawthorne, F.C. (2009) Crystal structure and Mössbauer spectroscopy of tschermakite from the ruby locality at Fiskenaesset, Greenland. The Canadian Mineralogist 47, 917-926.

Archanjo, C.J., Bouchez, J.-L., Corsini, M., and Vauchez, A. (1994) The Pombal granite pluton: magnetic fabric, emplacement and relationships with the Brasiliano strike-slip setting of NE Brazil (Paraiba State). Journal of Structural Geology 16, 323-335.

Ballet, O., and Coey, J.M.D. (1982) Magnetic properties of sheet silicates; 2:1 layer minerals. Physics and Chemistry of Minerals 8, 218-229.

Beausoleil, N., Lavallee, P., Yelon, A., Ballet, O., and Coey, J.M.D. (1983) Magnetic properties of biotite micas. Journal of Applied Physics 54, 906-915.

Bergmüller, F., Bärlocher, C., Geyer, B., Grieder, M., Heller, F., and Zweifel, P. (1994). A torque magnetometer for measurements of the high-field anisotropy of rocks and crystals. Measurement Science and Technology 5, 1466-1470.

Biedermann, A.R., Bender Koch, C., Lorenz, W.E.A., and Hirt, A.M. (2014a) Low-temperature magnetic anisotropy in micas and chlorite. Tectonophysics, doi: 10.1016/j.tecto.2014.01.015

Biedermann, A.R., Pettke, T., Reusser E., and Hirt, A.M. (2014b) Anisotropy of magnetic susceptibility in natural olivine single crystals. Geochemistry Geophysics Geosystems 15, 3051-3065 , doi: 10.1002/2014GC005386

Biedermann, A.R., Lowrie, W., and Hirt, A.M. (2013) A method for improving the measurement of low-field magnetic susceptibility anisotropy in weak samples. Journal of Applied Geophysics 88, 122-130.

Bleil, U., and Petersen, N. (1982) Magnetische Eigenschaften der Minerale, in: G. Angenheister (Ed.), Landolt-Börnstein - Numerical Data and Functional Relationships in Science and Technology - Group V: Geophysics and Space Research. Springer, Berlin.

Borradaile, G., Keeler, W., Alford, C., and Sarvas, P. (1987) Anisotropy of magnetic susceptibility of some metamorphic minerals. Physics of the Earth and Planetary Interiors 48, 161-166.

Borradaile, G.J., Stewart, R.A., and Werner, T. (1993). Archean uplift of a subprovince boundary in the Canadian Shield, revealed by magnetic fabrics. Tectonophysics 227, 1-15.

Burns, R.G. (1993) Mineralogical applications of crystal field theory, 2nd ed. 576p. Cambridge University Press, UK.

Deer, W.A., Howie, R.A., and Zussman, J. (1997) Double-chain silicates, 2nd ed. 784p. The Geological Society, London, UK.

Finke, W. (1909) Magnetische Messungen an Platinmetallen und monoklinen Kristallen, insbesondere der Eisen-, Kobalt- und Nickelsalze. Annalen der Physik 336, 149-168.

Guillong, M., Meier, D.L., Allan, M.M., Heinrich, C.A., and Yardley, B.W.D. (2008) SILLS: A MATLAB-based program for the reduction of laser ablation ICP-MS data of homogeneous materials and inclusions. Mineralogical Association of Canada Short Course 40, 328-333.

Hawthorne, F.C. (1983) The crystal chemistry of the amphiboles. The Canadian Mineralogist 21, 173-480.

Hrouda, F. (2004) Problems in interpreting AMS parameters in diamagnetic rocks. In: F. Martin-Hernandez, C.M. Lueneburg, C. Aubourg, and M. Jackson (eds) Magnetic Fabric: Methods and Applications. The Geological Society Special Publications 238, 49-59.

Jelinek, V. (1981) Characterization of the magnetic fabric of rocks. Tectonophysics 79, T63-T67.

Jelinek, V. (1984) On a mixed quadratic invariant of the magnetic susceptibility tensor. Journal of Geophysics - Zeitschrift Fur Geophysik 56, 58-60.

Lagroix, F., and Borradaile, G.J. (2000) Magnetic fabric interpretation complicated by inclusions in mafic silicates. Tectonophysics 325, 207-225.

Laugier, J., and Filhol, A. (1983). An interactive program for the interpretation and simulation of Laue patterns. Journal of Applied Crystallography 16, 281-283.

Martín-Hernández, F., and Hirt, A.M. (2001) Separation of ferrimagnetic and paramagnetic anisotropies using a high-field torsion magnetometer. Tectonophysics 337, 209-221.

Martín-Hernández, F., and Hirt, A.M. (2004) A method for the separation of paramagnetic, ferrimagnetic and haematite magnetic subfabrics using high-field torque magnetometry. Geophysical Journal International 157, 117-127.

Neumann, F.E. (1885) Vorlesungen über die Theorie der Elastizität der festen Körper und des Lichtäthers. 374p. B.G. Teubner Verlag, Leipzig, Germany.

Nye, J.F. (1957) Physical Properties of Crystals: Their Representation by Tensors and Matrices. 338p. Clarendon Press, Oxford, UK.

Oberti, R., Hawthorne, F.C., Cannillo, E., and Camara, F. (2007) Long-range order in amphiboles. In: Keppler H., Smyth, J.R. (eds) Reviews in Mineralogy and Geochemistry 67, 125-171.

Parks, G.A., and Akhtar, S. (1968) Magnetic moment of Fe^{2+} in paramagnetic minerals. The American Mineralogist 53, 406-415.

Parry, G.R. (1971). The magnetic anisotropy of some deformed rocks. 218p. PhD thesis, University of Birmingham, Birmingham, UK.

Pettke, T., Oberli, F., Audetat, A., Guillong, M., Simon, A., Hanley, J., and Klemm, L.M. (2012) Recent developments in element concentration and isotope ratio analysis of individual fluid inclusions by laser ablation single and multiple collector ICP–MS. Ore Geology Reviews 44, 10-38.

Reusser, C.E. (1987) Phasenbeziehungen im Tonalit der Bergeller Intrusion. PhD thesis, Department of Earth Sciences. ETH Zurich, Zurich, Switzerland.

Schmidt, V., Hirt, A.M., Hametner, K., and Gunther, D. (2007a) Magnetic anisotropy of carbonate minerals at room temperature and 77 K. American Mineralogist 92, 1673-1684.

Schmidt, V., Hirt, A.M., Rosselli, P., and Martín-Hernández, F. (2007b) Separation of diamagnetic and paramagnetic anisotropy by high-field, low-temperature torque measurements. Geophysical Journal International 168, 40-47.

Schulmann, K., and Ježek, J. (2011) Some remarks on fabric overprints and constrictional AMS fabrics in igneous rocks. International Journal of Earth Sciences 101, 705-714.

Spandler, C., Pettke, T., and Rubatto, D. (2011) Internal and external fluid sources for eclogite-facies veins in the Monviso Meta-ophiolite, Western Alps: Implications for fluid flow in subduction zones. Journal of Petrology 52, 1207-1236.

Vernon, R.H. (1961) Magnetic susceptibility as a measure of total iron plus manganese in some ferromagnesian silicate minerals. The American Mineralogist 46, 1141-1153.

Verwey, E.J.W. (1939) Electronic conduction of magnetite (Fe_3O_4) and its transition point at low temperatures. Nature 144, 327-328.

Wagner, J.-J., Hedley, I.G., Steen, D., Tinkler, C., and Vuagnat, M. (1981) Magnetic anisotropy and fabric of some progressively deformed ophiolitic gabbros. Journal of Geophysical Research 86, 307-315.

Walz, F. (2002) The Verwey transition - a topical review. Journal of Physics: Condensed Matter 14, R285-R340.

644 Zak, J., Verner, K., and Tycova, P. (2008) Multiple magmatic fabrics in plutons: an
645 overlooked tool for exploring interactions between magmatic processes and regional
646 deformation? Geological Magazine 145, 537-551.

647

648

649 Figure 1. Crystal structure and site locations for amphiboles (figure generated using
650 CrystalMaker).

651 Figure 2. Characteristic Mössbauer spectra and fits for selected amphibole crystals. Numbers
652 refer to Components 1, 2 and 3 discussed in the text and shown in Table 2.

653 Figure 3. Acquisition of IRM for representative samples. Note the different scale for
654 hornblende compared to the other amphibole minerals.

655 Figure 4. Mass susceptibility as a function of Fe concentration. Open circles represent
656 samples with significant ferromagnetic contributions from mineral or melt inclusions.
657 Samples represented by filled circles are considered purely paramagnetic or diamagnetic.
658 Solid and dashed lines represent the susceptibility increase as defined by Eq. 1, and the
659 theoretical increase, respectively.

660 Figure 5. Lower hemisphere equal-area stereoplots showing the directions of principal
661 susceptibilities for minerals in the amphibole group. Left column shows principal directions
662 of the low-field AMS, middle and right column are paramagnetic principal directions isolated
663 from high-field data at room temperature (RT) and 77 K, respectively. Susceptibility
664 directions are given in a crystallographic reference frame.

665 Figure 6. Modified Jelinek plot showing AMS shape U as a function of k' for (a) low-field
666 AMS, and (b) dia-/paramagnetic AMS extracted from high-field AMS.

667 Figure 7. Paramagnetic anisotropy degree k' as a function of Fe concentration.

668 Figure 8. Low-temperature magnetization curves for selected samples. Symbols correspond to
669 measured susceptibility along the a^*, b and c crystallographic axes. Solid lines are the
670 corresponding Curie-Weiss fits. The black arrow indicates a magnetic transition in Amph3.

671 Figure 9. The ratio of the anisotropy degree at 77 K to that at room temperature (p'_{77}) as a
672 function of Fe concentration.

673

674

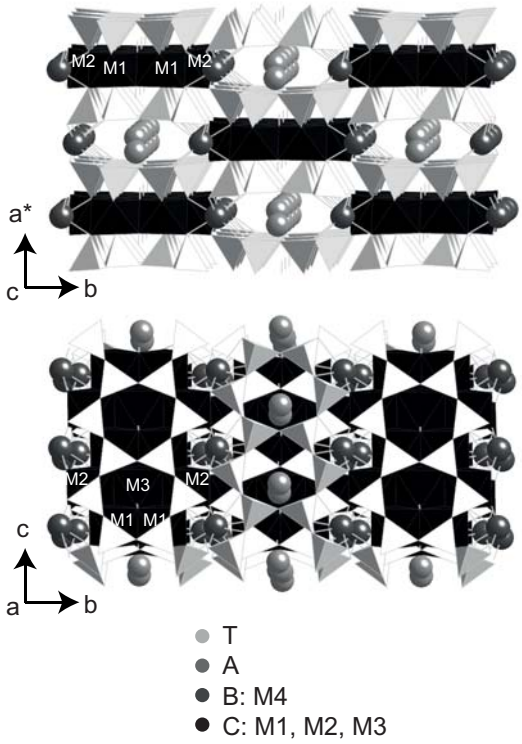
M2
M1
M1
M2
a*
c
b
M2
M3
M2
M1
M1
c
a
b
T
A
B: M4
C: M1, M2, M3

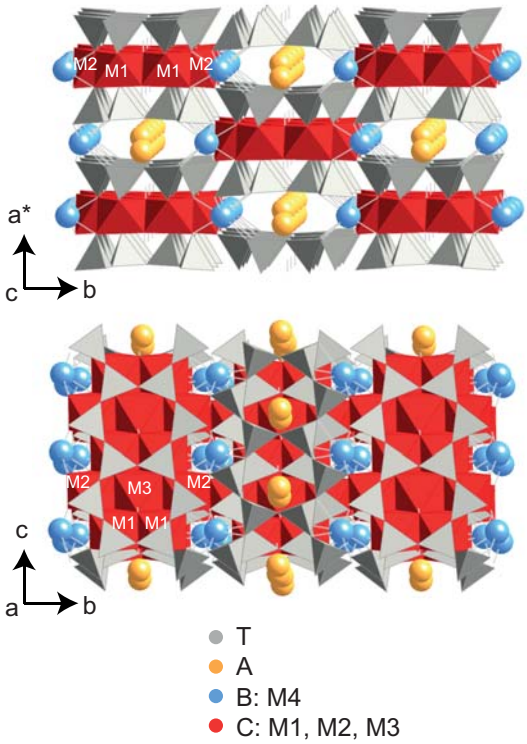
M2
M1
M1
M2
a*
c
b
M2
M3
M2
M1
M1
c
a
b
T
A
B: M4
C: M1, M2, M3

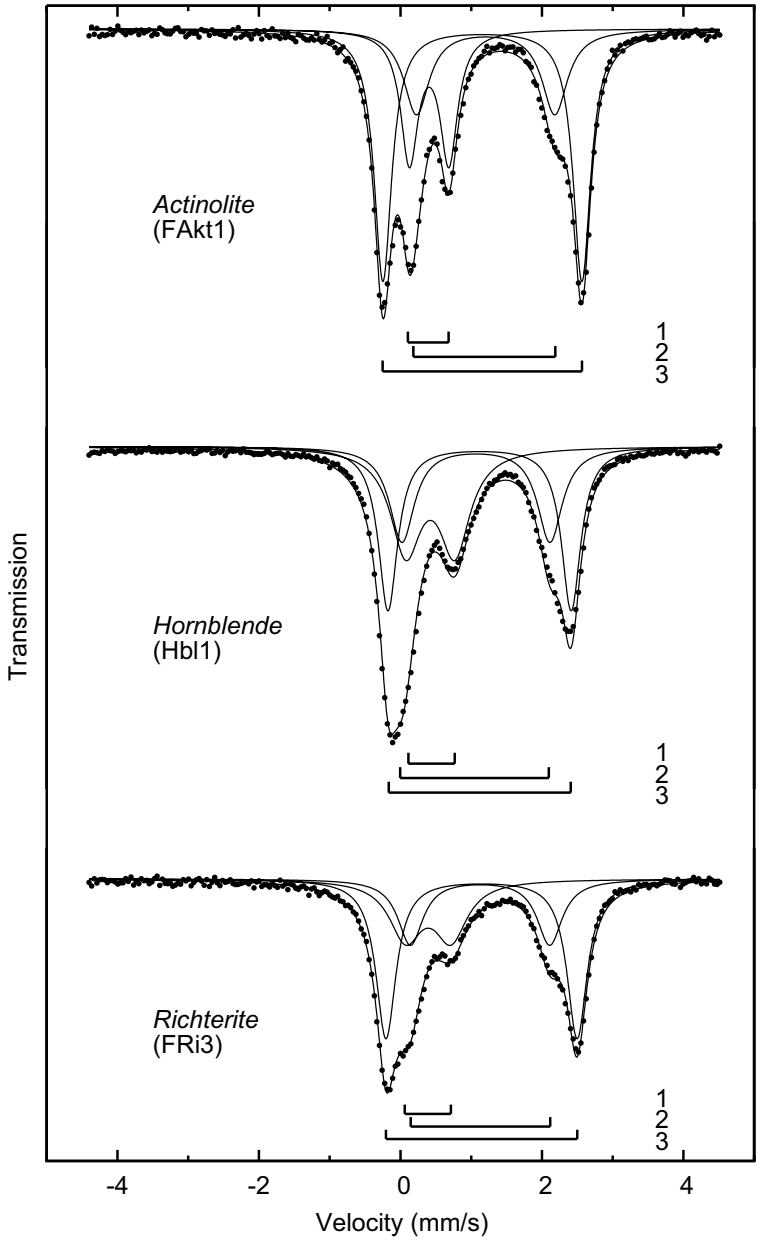
Actinolite
(FAkt1)
1
2
3
Hornblende
(Hbl1)
1
2
3
Richterite
(FRi3)
1
2
3
Transmission
-4
-2
0
2
4
Velocity (mm/s)

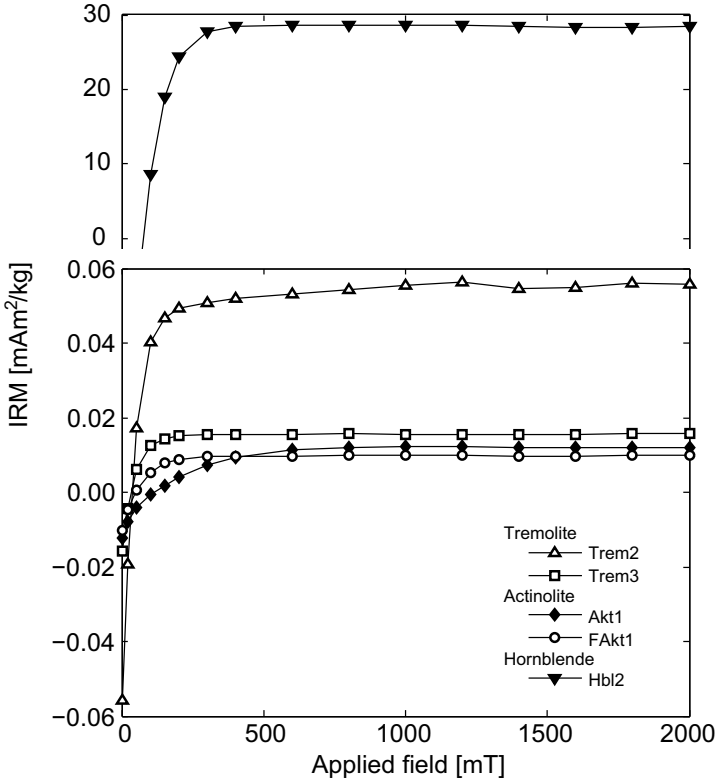
30
20
10
0
0.06
0.04
0.02
0.00
−0.02
−0.04
−0.06
IRM [mAm²/kg]
0
500
1000
1500
2000
Applied field [mT]
Tremolite
Trem2
Trem3
Actinolite
Akt1
FAkt1
Hornblende
Hbl2

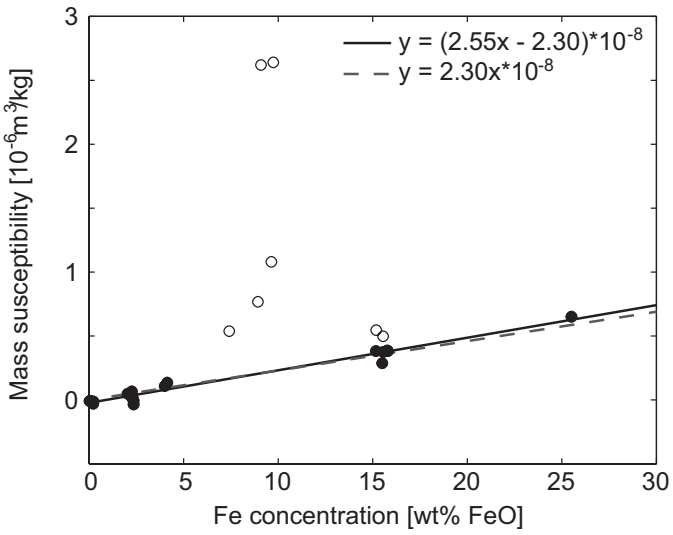
y = (2.55x - 2.30)*10^-8
y = 2.30x*10^-8
Mass susceptibility [10^-6 m^3/kg]
Fe concentration [wt% FeO]
0
1
2
3
0
5
10
15
20
25
30

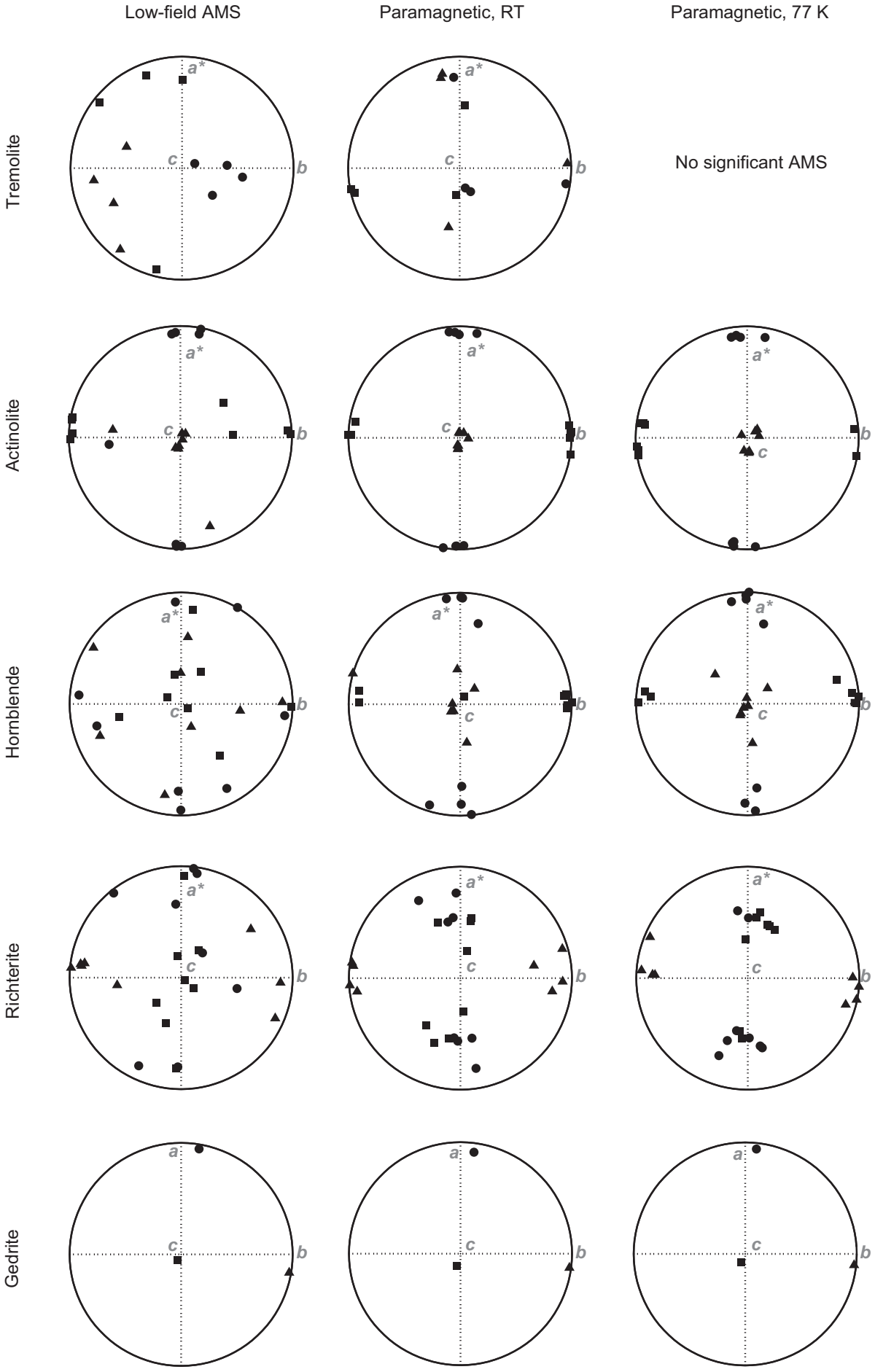
High-field AMS
Low-field AMS
Paramagnetic, RT
Paramagnetic, 77 K
Tremolite
No significant AMS
Actinolite
Hornblende
Richterite
Gedrite
a*
a
b
c

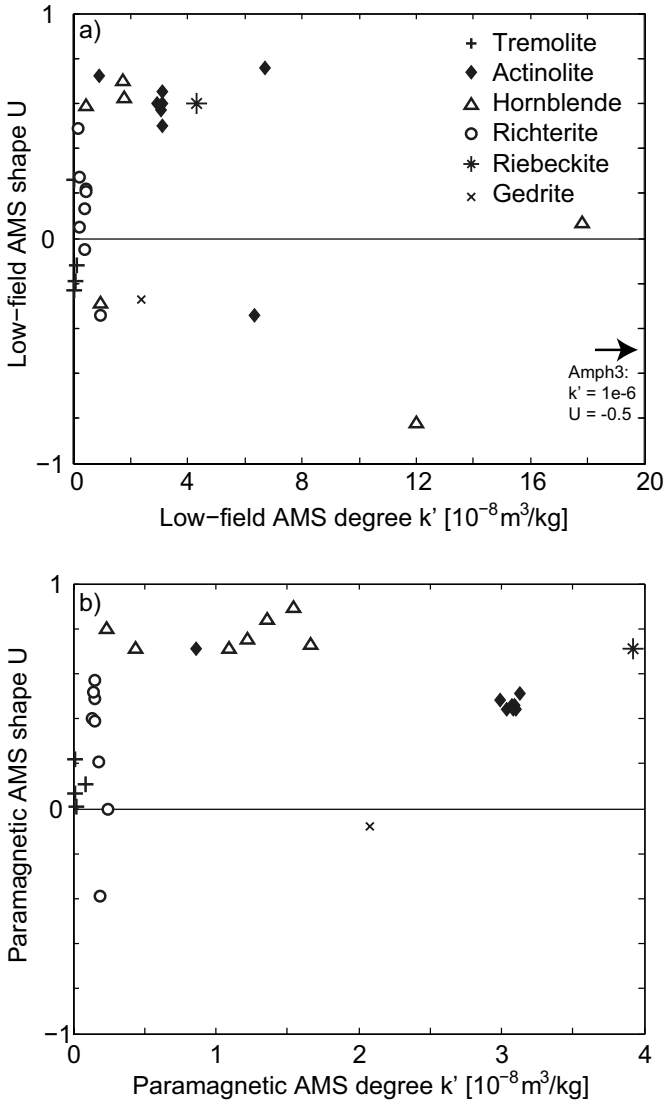
a)
Tremolite
Actinolite
Hornblende
Richterite
Riebeckite
Gedrite
Amph3:
k' = 1e-6
U = -0.5
Low−field AMS shape U
Low−field AMS degree k' [10−8m3/kg]
b)
Paramagnetic AMS shape U
Paramagnetic AMS degree k' [10−8m3/kg]

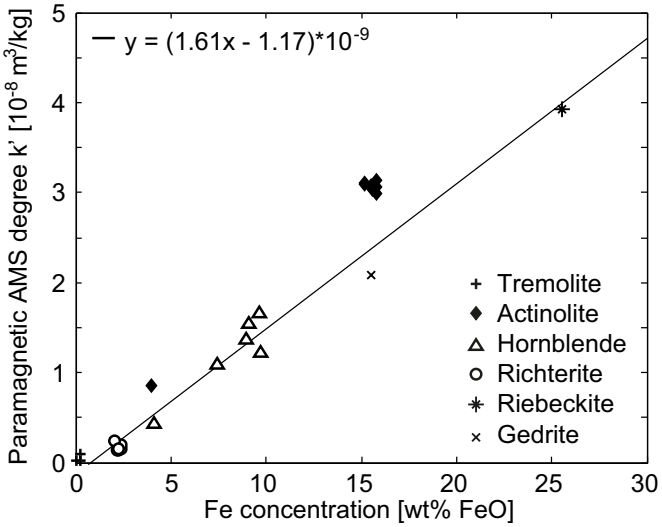
y = (1.61x - 1.17)*10^-9
Paramagnetic AMS degree k' [10^-8 m^3/kg]
Fe concentration [wt% FeO]
Tremolite
Actinolite
Hornblende
Richterite
Riebeckite
Gedrite
0
1
2
3
4
5
0
5
10
15
20
25
30

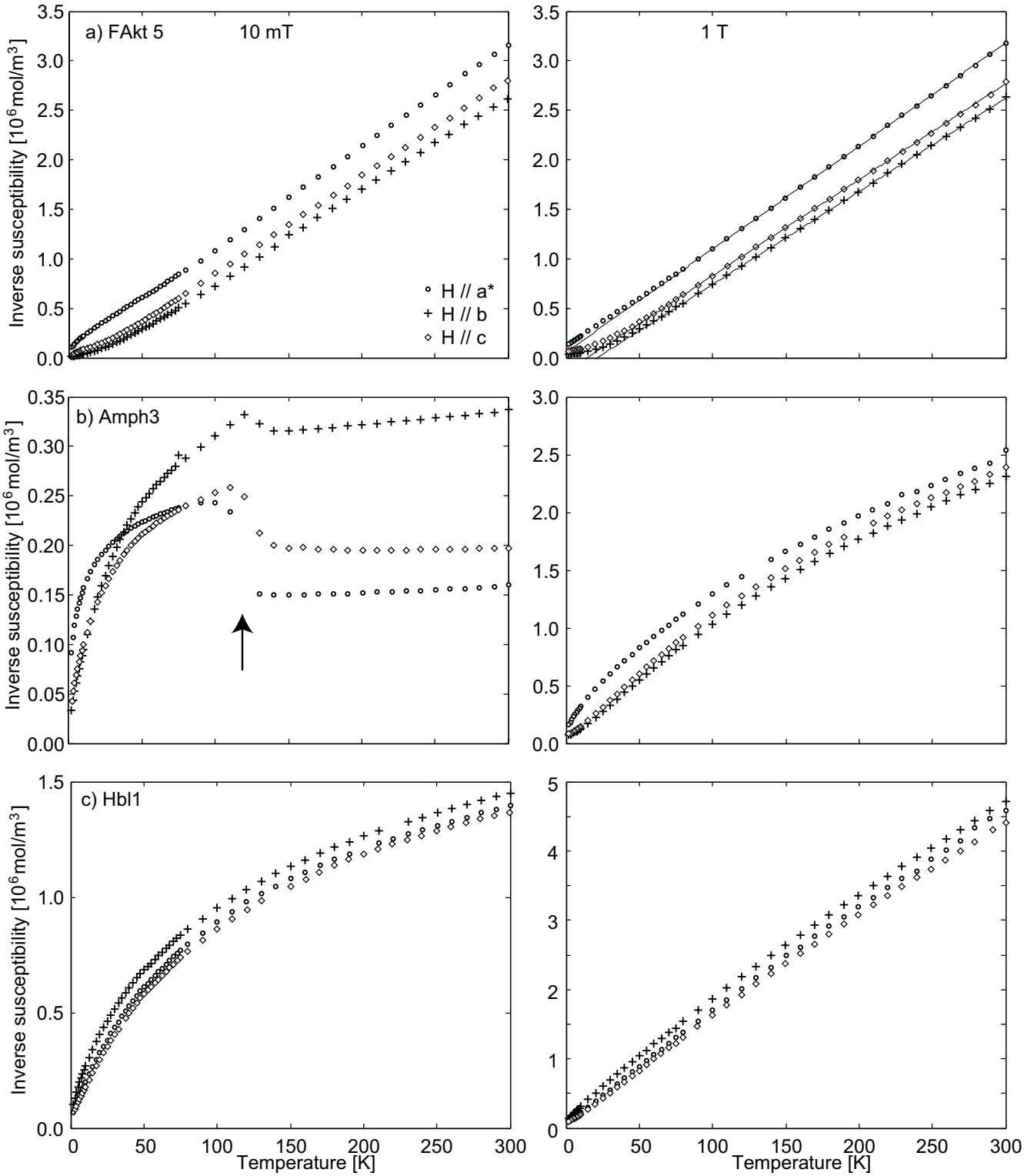
a) FAkt 5
10 mT
1 T
H // a*
H // b
H // c
b) Amph3
c) Hbl1
Inverse susceptibility [10^6 mol/m^3]
Temperature [K]

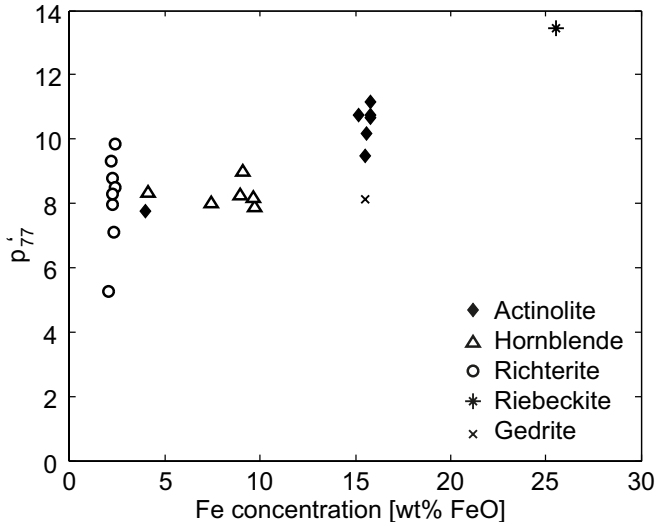
14
12
10
8
6
4
2
0
0
5
10
15
20
25
30
p_{77}'
Fe concentration [wt% FeO]
Actinolite
Hornblende
Richterite
Riebeckite
Gedrite

Table1: Mineral samples included in this study: Sample name, mass, mineral and locality

Mineral grou	Sample	Mass (g)	Mineral	Locality
Clinoamphiboles:				
Calcic amphiboles				
Tremolite				
	Trem1	1.08	tremolite	unknown
	Trem2	0.38	tremolite	unknown
	Trem3	1.22	tremolite	Merelani, Tanzania
	Trem4	1.03	tremolite	Merelani, Tanzania
Actinolite				
	Akt1	2.21	actinolite	unknown
	FAkt1	1.87	ferroactinolite	Chigar Valley, Baltistan, Pakistan
	FAkt2	5.13	ferroactinolite	Chigar Valley, Baltistan, Pakistan
	FAkt3	5.09	ferroactinolite	Chigar Valley, Baltistan, Pakistan
	FAkt4	4.72	ferroactinolite	Chigar Valley, Baltistan, Pakistan
	FAkt5	4.17	ferroactinolite	Chigar Valley, Baltistan, Pakistan
	FAkt6	4.19	ferroactinolite	Chigar Valley, Baltistan, Pakistan
	FAkt7	5.58	ferroactinolite	Chigar Valley, Baltistan, Pakistan
Hornblende				
	Amph	1.46	pargasite	unknown
	Amph1	7.56	hornblende with intergrowths	unknown
	Amph3	0.38	pargasite	unknown
	Amph5	0.98	pargasite	Lodmurwak Maar, Tanzania
	Hbl1	3.01	pargasite	unknown
	Hbl2	7.96	pargasite	Twin Peaks, Yakima, Washingon, US
	NMB535	5.66	pargasite	Teplice, Böhmen, Czech Republic
Sodic-calcic amphiboles				
Richterite				
	FRi1	1.50	fluororichterite	Essenville Rd., Wilberforce, Ontario, Canada
	FRi2	0.33	fluororichterite	Essenville Rd., Wilberforce, Ontario, Canada
	FRi3	0.28	fluororichterite	Essenville Rd., Wilberforce, Ontario, Canada
	FRi4	0.12	fluororichterite	Essenville Rd., Wilberforce, Ontario, Canada

FRi5	0.16	fluororichterite	Essenville Rd., Wilberforce, Ontario, Canada
NMB45532a	1.60	fluororichterite	Sunset Park Road, Bancroft, Québec, Canada
NMB45532b	1.17	fluororichterite	Sunset Park Road, Bancroft, Québec, Canada
Amph2	3.64	richterite	unknown

Sodic amphiboles

Riebeckite

NMB44662[a]	5.48	riebeckite	St Peters Dome, El Paso County, Colorado, US

Orthoamphiboles:

Fe-Mg-Mn amphiboles

Gedrite

NMB25424	0.31	gedrite	Alp i Mondei, Val Antrona, Verbano-Cusio-Ossola, Piemont, Italy

[a] This sample is an aggregate of fibrous grains.

Table 2: Hyperfine parameters and relative areas of ferrous and ferric iron and site occupancies for Fe2+ as determined from Mössbauer spectroscopy.

	Component 1 (Fe^{3+})				Component 2 (Fe^{2+} in M2 sites)				Component 3 (Fe^{2+} in M1, M3)		
Sample	Isomer shift (mm/s)	Quadrupole splitting (mm/s)	Line width (mm/s)	Area (%)	Isomer shift (mm/s)	Quadrupole splitting (mm/s)	Line width (mm/s)	Area (%)	Isomer shift (mm/s)	Quadrupole splitting (mm/s)	Line width (mm/s)
Clinoamphiboles:											
Calcic amphiboles											
Tremolite											
Trem2	0.45	0.26	0.22	13	1.10	1.92	0.43	44	1.15	2.82	0.33
Actinolite											
FAkt1	0.44	0.49	0.30	27	1.14	2.11	0.46	26	1.16	2.82	0.29
FAkt4	0.45	0.49	0.32	24	1.13	2.08	0.41	25	1.16	2.82	0.29
Hornblende											
Amph	0.41	0.74	0.54	40	1.08	2.14	0.43	30	1.12	2.60	0.33
Amph3	0.39	0.71	0.46	37	1.09	2.18	0.47	28	1.13	2.65	0.30
Amph5	0.38	0.78	0.55	41	1.10	2.09	0.42	26	1.12	2.60	0.34
Hbl1	0.42	0.78	0.56	49	1.08	2.18	0.42	27	1.11	2.61	0.32
Hbl2	0.43	0.68	0.52	36	1.06	2.09	0.42	26	1.12	2.58	0.34
Sodic-calcic amphiboles											
Richterite											
FRi2	0.38	0.68	0.56	29	1.15	2.01	0.45	26	1.15	2.74	0.33
FRi3	0.43	0.58	0.54	27	1.10	2.05	0.46	28	1.15	2.71	0.33
FRi4	0.36	0.68	0.55	29	1.15	1.99	0.45	26	1.15	2.73	0.34
Amph2	0.38	0.65	0.60	32	1.11	1.99	0.41	24	1.15	2.70	0.33

Accuracies are ± 0.02 mm/s and ±2%

Area (%)	Fe2+/Fe3+
43	6.5
47	2.8
51	3.3
30	1.5
34	1.7
33	1.4
23	1.0
38	1.8
44	2.4
45	2.7
45	2.4
44	2.1

Table3: Low-field AMS with measured and calculated mean susceptibility, eigenvalues and directions of the principal susceptibility axes, and anisotropy parameters.

	Mass χ	Theoretical χ	Maximum axis			Intermediate axis			Minimum axis			AMS shape	AMS degree	Significance	
Sample	**(m3/kg)**	**(m3/kg)**	**k1**	**D1 (°)**	**I1 (°)**	**k2**	**D2 (°)**	**I2 (°)**	**k3**	**D3 (°)**	**I3 (°)**	**U**	**k' (m3/kg)**	**P**	**R1**
Clinoamphiboles:															
Calcic amphiboles															
Tremolite															
Trem1	-1.17E-08	5.20E-09	1.041	0.8	20.4	1.008	262.5	21.1	0.952	130.8	59.9	0.26	4.27E-10	1.09	0.5
Trem2	-2.99E-08	5.07E-09	1.035	339.8	10.2	0.996	243.3	32.4	0.970	85.1	55.6	-0.19	7.96E-10	1.07	0.4
Trem3	-8.83E-09	6.86E-10	1.053	194.7	6.5	0.992	291.2	44.8	0.955	98.3	44.5	-0.23	3.59E-10	1.10	0.6
Trem4	-6.76E-09	1.27E-09	1.243	308.3	4.8	0.981	217.6	8.3	0.776	67.7	80.4	-0.12	1.29E-09	1.60	2.2
Actinolite															
Akt1	1.09E-07	9.21E-08	1.071	280.8	2.2	1.045	125.6	87.6	0.884	10.9	1.0	0.72	9.02E-09	1.21	23.4
FAkt1	3.83E-07	3.64E-07	1.076	279.7	0.7	1.038	183.4	84.0	0.887	9.8	5.9	0.60	3.12E-08	1.21	31.2
FAkt2	3.85E-07	3.63E-07	1.071	272.5	3.3	1.035	47.5	85.3	0.894	182.3	3.3	0.60	2.94E-08	1.20	45.3
FAkt3	3.86E-07	3.63E-07	1.079	269.5	1.0	1.032	15.6	86.3	0.889	179.5	3.6	0.50	3.12E-08	1.21	126.9
FAkt4	5.46E-07	3.49E-07	1.155	50.1	48.6	0.969	161.5	17.9	0.876	265.0	35.9	-0.34	6.35E-08	1.32	90.7
FAkt5	3.83E-07	3.49E-07	1.075	87.8	0.8	1.035	185.9	84.5	0.889	357.7	5.4	0.57	3.06E-08	1.21	78.7
FAkt6	3.76E-07	3.58E-07	1.074	85.4	4.6	1.041	211.5	82.3	0.885	354.9	6.2	0.65	3.10E-08	1.21	119.2
FAkt7	4.98E-07	3.58E-07	1.113	87.1	51.4	1.076	276.3	38.2	0.811	182.8	4.5	0.76	6.71E-08	1.37	79.5
Hornblende															
Amph	2.64E-06	2.24E-07	1.081	143.4	41.5	1.004	5.6	40.0	0.916	255.1	22.7	0.07	1.78E-07	1.18	48.8
Amph1	1.35E-07	9.52E-08	1.030	91.4	0.9	1.015	359.3	67.2	0.956	181.8	22.8	0.59	4.31E-09	1.08	27.3
Amph3	2.62E-06	2.09E-07	1.529	348.5	68.0	0.851	189.0	20.8	0.620	96.3	7.0	-0.49	1.01E-06	2.46	315.6
Amph5	1.08E-06	2.22E-07	1.156	31.3	62.9	0.933	248.3	22.3	0.911	152.1	14.7	-0.82	1.20E-07	1.27	94.8
Hbl1	5.38E-07	1.71E-07	1.030	289.5	78.7	1.016	89.9	10.6	0.955	180.6	3.7	0.62	1.76E-08	1.08	32.9
Hbl2	7.68E-07	2.06E-07	1.020	258.8	43.2	1.012	96.0	45.4	0.969	357.0	8.7	0.70	1.72E-08	1.05	21.2
NMB535	5.08E-07		1.025	284.0	83.9	0.996	79.8	5.6	0.980	170.1	2.5	-0.29	9.40E-09	1.05	6.8
Sodic-calcic amphiboles															
Richterite															
FRi1	3.46E-08	5.13E-08	1.070	32.5	66.8	1.002	276.5	10.6	0.928	182.5	20.4	0.05	2.01E-09	1.15	1.2
FRi2	2.31E-08	5.27E-08	1.106	133.4	78.4	1.021	277.3	9.4	0.874	8.5	6.7	0.27	2.22E-09	1.27	0.7
FRi3	1.92E-08	5.22E-08	1.261	348.6	74.4	1.042	113.8	9.1	0.698	205.8	12.6	0.22	4.45E-09	1.81	1.0
FRi4	-3.47E-08	5.42E-08	1.141	1.2	8.6	0.995	263.6	40.9	0.863	100.8	47.8	-0.05	3.94E-09	1.32	0.5
FRi5	-6.36E-09	5.43E-08	1.805	183.6	19.0	1.118	278.2	13.0	0.076	40.6	66.7	0.21	4.52E-09	23.63	0.6
NMB45532a	4.37E-08	4.93E-08	1.032	199.3	53.5	1.012	93.1	11.6	0.956	355.1	34.0	0.49	1.40E-09	1.08	2.7
NMB45532b	4.81E-08	4.70E-08	1.097	225.8	64.4	1.009	52.6	25.4	0.894	321.3	2.6	0.13	3.98E-09	1.23	4.1
Amph2	6.64E-08	5.20E-08	1.191	110.1	86.6	0.961	276.6	3.3	0.848	6.6	0.8	-0.34	9.50E-09	1.41	27.7
Sodic amphiboles															
Riebeckite															
NMB44662	6.51E-07	5.87E-07	1.062			1.031			0.908			0.60	4.33E-08	1.17	42.0
Orthoamphiboles:															
Fe-Mg-Mn amphiboles															
Gedrite															
NMB25424	2.87E-07	3.57E-07	1.110	226.9	85.2	0.982	99.2	3.0	0.909	9.0	3.8	-0.27	2.38E-08	1.22	5.2

Table 4: High-field AMS with eigenvalues, directions of the principal susceptibility axes, and anisotropy parameters of the dia-/paramagnetic deviatoric susceptibility at room temperature and at 77 K. Ferromagnetic results are only shown when significant.

Paramagnetic component			Maximum axis		Intermediate axis			Minimum axis			AMS shape			
Sample	Temperature	%para	k1 (m3/kg)	D1 (°)	I1 (°)	k2 (m3/kg)	D2 (°)	I2 (°)	k3 (m3/kg)	D3 (°)	I3 (°)	U	k' (m3/kg)	p77'
Clinoamphiboles:														
Calcic amphiboles														
Tremolite														
Trem1	RT	80 ± 57	1.05E-09	187.7	70.1	8.06E-11	87.5	3.7	-1.13E-09	356.2	19.6	0.11	8.92E-10	
Trem1	77 K	Anisotropy not significant												
Trem2	RT	75 ± 1309	2.48E-10	4.3	43.7	1.37E-12	193.5	45.9	-2.49E-10	98.7	4.6	0.01	2.03E-10	
Trem2	77 K	Anisotropy not significant												
Trem3	RT	84 ± 36	1.73E-10	259.4	1.5	2.68E-11	349.7	14.5	-2.00E-10	163.7	75.4	0.22	1.53E-10	
Trem3	77 K	Anisotropy not significant												
Trem4	RT	65 ± 38	2.04E-10	256.9	4.1	1.03E-11	348.3	18.0	-2.14E-10	154.5	71.5	0.07	1.71E-10	
Trem4	77 K	Anisotropy not significant												
Actinolite														
Akt1	RT	92 ± 5	7.46E-09	278.6	6.2	4.59E-09	96.2	83.7	-1.20E-08	188.6	0.3	0.71	8.58E-09	7.75
Akt1	77 K	91 ± 17	5.64E-08	277.3	8.5	3.70E-08	82.2	81.2	-9.34E-08	187.0	2.3	0.74	6.65E-08	
FAkt1	RT	86 ± 177	3.06E-08	98.9	0.7	1.24E-08	195.4	83.4	-4.30E-08	8.9	6.5	0.51	3.13E-08	11.15
FAkt1	77 K	94 ± 75	3.36E-07	99.9	1.2	1.45E-07	196.4	79.7	-4.81E-07	9.7	10.2	0.53	3.49E-07	
FAkt2	RT	94 ± 177	2.96E-08	272.2	2.4	1.13E-08	32.0	85.2	-4.10E-08	182.0	4.2	0.48	2.99E-08	10.75
FAkt2	77 K	88 ± 178	3.11E-07	93.3	2.1	1.32E-07	266.0	87.9	-4.43E-07	3.2	0.3	0.53	3.22E-07	
FAkt3	RT	93 ± 68	3.07E-08	271.7	0.5	1.12E-08	9.9	86.2	-4.19E-08	181.6	3.8	0.46	3.07E-08	10.65
FAkt3	77 K	89 ± 112	3.22E-07	92.2	1.3	1.26E-07	353.5	81.8	-4.48E-07	182.4	8.1	0.49	3.27E-07	
FAkt4	RT	85 ± 147	3.10E-08	89.6	2.0	1.13E-08	194.0	82.1	-4.22E-08	359.3	7.7	0.46	3.09E-08	10.74
FAkt4	77 K	92 ± 25	3.34E-07	88.9	4.4	1.20E-07	220.0	83.4	-4.53E-07	358.5	5.0	0.46	3.32E-07	
FAkt5	RT	95 ± 48	3.14E-08	87.1	0.3	1.08E-08	180.3	83.6	-4.23E-08	357.1	6.4	0.44	3.10E-08	10.76
FAkt5	77 K	94 ± 68	3.33E-07	89.8	4.1	1.23E-07	204.3	80.2	-4.57E-07	359.2	8.9	0.47	3.34E-07	
FAkt6	RT	95 ± 56	3.09E-08	84.0	2.9	1.05E-08	201.1	83.6	-4.14E-08	353.7	5.7	0.44	3.04E-08	10.17
FAkt6	77 K	87 ± 30	3.01E-07	84.3	2.3	1.25E-07	186.3	79.0	-4.26E-07	353.9	10.8	0.52	3.10E-07	
FAkt7	RT	94 ± 32	3.11E-08	87.8	0.5	1.08E-08	349.8	86.3	-4.19E-08	177.9	3.7	0.44	3.08E-08	9.47
FAkt7	77 K	81 ± 613	2.86E-07	85.4	3.8	1.14E-07	296.3	85.6	-4.00E-07	175.6	2.3	0.50	2.91E-07	
Hornblende														
Amph	RT	89 ± 71	1.03E-08	84.3	6.0	6.86E-09	277.5	83.9	-1.72E-08	174.4	1.4	0.75	1.22E-08	7.90
Amph	77 K	89 ± 34	8.00E-08	86.0	0.7	5.59E-08	348.0	85.2	-1.36E-07	176.1	4.7	0.78	9.66E-08	
Amph1	RT	88 ± 15	3.79E-09	89.2	1.1	2.34E-09	357.1	62.9	-6.14E-09	179.7	27.1	0.71	4.38E-09	8.31
Amph1	77 K	76 ± 72	3.09E-08	74.9	19.7	2.02E-08	310.9	57.3	-5.11E-08	174.5	24.9	0.74	3.64E-08	
Amph3	RT	15 ± 3	1.18E-08	26.7	84.1	9.91E-09	287.2	1.0	-2.17E-08	197.1	5.8	0.89	1.54E-08	8.97
Amph3	77 K	72 ± 13	1.20E-07	270.5	1.6	7.27E-08	99.2	88.4	-1.93E-07	0.5	0.3	0.70	1.38E-07	
Amph5	RT	72 ± 47	1.42E-08	271.5	10.3	9.09E-09	41.7	74.2	-2.33E-08	179.4	11.8	0.73	1.66E-08	8.18
Amph5	77 K	82 ± 81	1.13E-07	274.6	13.9	7.85E-08	51.3	71.2	-1.92E-07	181.5	12.4	0.78	1.36E-07	
Hbl1	RT	91 ± 7	9.43E-09	84.2	5.1	5.80E-09	234.8	84.1	-1.52E-08	354.0	2.9	0.71	1.09E-08	8.00
Hbl1	77 K	89 ± 35	7.34E-08	83.0	4.2	4.86E-08	208.4	82.7	-1.22E-07	352.6	5.9	0.75	8.69E-08	
Hbl2	RT	93 ± 95	1.08E-08	91.8	4.6	8.46E-09	225.2	83.3	-1.92E-08	1.4	4.9	0.84	1.36E-08	8.23
Hbl2	77 K	94 ± 231	9.03E-08	89.4	2.7	6.78E-08	225.9	86.2	-1.58E-07	359.2	2.6	0.82	1.12E-07	
NMB535	RT	87 ± 5	1.95E-09	90.6	5.2	1.42E-09	226.4	82.8	-3.37E-09	0.1	5.0	0.80	2.39E-09	7.29
NMB535	77 K	91 ± 22	1.41E-08	89.7	5.3	1.04E-08	215.2	81.0	-2.46E-08	359.0	7.3	0.81	1.74E-08	
Sodic-calcic amphiboles														
Richterite														

FRi1	RT	97 ±	61	1.46E-09	10.8	44.7	5.66E-10	278.1	2.7	-2.02E-09	185.4	45.2	0.49	1.48E-09	8.77
FRi1	77 K	90 ±	110	1.40E-08	11.2	39.9	3.19E-09	101.2	0.1	-1.72E-08	191.3	50.1	0.31	1.29E-08	
FRi2	RT	88 ±	100	2.01E-09	176.1	65.9	3.08E-10	266.6	0.2	-2.31E-09	356.7	24.1	0.21	1.78E-09	7.09
FRi2	77 K	72 ±	667	1.31E-08	28.4	48.5	3.90E-09	293.0	4.8	-1.70E-08	198.8	41.1	0.39	1.26E-08	
FRi3	RT	87 ±	313	1.42E-09	338.5	44.6	5.92E-10	73.7	5.3	-2.01E-09	168.9	44.9	0.52	1.46E-09	7.96
FRi3	77 K	43 ±	100	1.27E-08	20.1	47.1	2.76E-09	272.4	15.7	-1.54E-08	169.4	38.6	0.29	1.16E-08	
FRi4	RT	81 ±	130	1.47E-09	202.3	37.7	6.90E-10	97.8	18.0	-2.16E-09	347.6	46.8	0.57	1.56E-09	9.86
FRi4	77 K	61 ±	1097	1.81E-08	357.6	61.4	1.32E-09	105.2	9.4	-1.95E-08	199.9	26.7	0.11	1.54E-08	
FRi5	RT	84 ±	508	2.59E-09	14.6	69.5	-5.94E-10	262.5	8.0	-2.00E-09	169.8	18.8	-0.39	1.92E-09	8.49
FRi5	77 K	49 ±	136	1.70E-08	23.7	48.0	5.01E-09	271.9	18.5	-2.20E-08	167.8	36.1	0.39	1.63E-08	
NMB45532a	RT	93 ±	18	1.39E-09	190.9	43.7	4.28E-10	92.1	9.1	-1.82E-09	353.0	44.9	0.40	1.35E-09	9.33
NMB45532a	77 K	90 ±	63	1.45E-08	186.1	45.3	1.65E-09	93.0	3.1	-1.61E-08	0.0	44.6	0.16	1.25E-08	
NMB45532b	RT	49 ±	360	2.94E-09	216.1	46.6	-4.79E-12	78.4	35.0	-2.93E-09	331.7	22.3	0.00	2.40E-09	5.25
NMB45532b	77 K	86 ±	87	1.45E-08	188.7	49.8	1.74E-09	88.5	8.6	-1.62E-08	351.5	38.9	0.17	1.26E-08	
Amph2	RT	74 ±	19	1.59E-09	9.8	47.7	4.71E-10	275.9	3.5	-2.06E-09	182.7	42.0	0.39	1.53E-09	8.28
Amph2	77 K	93 ±	30	1.45E-08	8.3	45.0	1.85E-09	273.6	4.6	-1.63E-08	179.0	44.6	0.18	1.26E-08	
Sodic amphiboles															
Riebeckite															
NMB44662	RT	96 ±	35	3.39E-08			2.11E-08			-5.50E-08			0.71	3.92E-08	13.44
NMB44662	77 K	96 ±	41	4.43E-07			2.98E-07			-7.41E-07			0.76	5.27E-07	
Orthoamphiboles:															
Fe-Mg-Mn amphiboles															
Gedrite															
NMB25424	RT	71 ±	269	2.62E-08	200.0	80.2	-1.42E-09	97.6	2.1	-2.48E-08	7.3	9.6	-0.08	2.08E-08	8.12
NMB25424	77 K	89 ±	19	2.12E-07	207.0	83.0	-1.01E-08	96.1	2.5	-2.02E-07	5.8	6.5	-0.07	1.69E-07	

Ferromagnetic component			**Maximum axis**			**Intermediate axis**			**Minimum axis**			**AMS shape**	
Sample	**Temperature**	**%ferro**	**k1 (m3/kg)**	**D1 (°)**	**I1 (°)**	**k2 (m3/kg)**	**D2 (°)**	**I2 (°)**	**k3 (m3/kg)**	**D3 (°)**	**I3 (°)**	**U**	**k' (m3/kg**
Calcic amphiboles													
Actinolite													
Akt1	RT	8 ±	4	8.87E-10	140.4	24.3	1.48E-10	283.8	60.7	-1.03E-09	43.2	15.4	0.23	7.89E-10
Hornblende													
Amph1	RT	12 ±	11	7.22E-10	144.2	57.2	3.40E-11	277.4	23.8	-7.57E-10	17.3	21.1	0.07	6.04E-10
Amph3	RT	85 ±	9	1.02E-07	4.2	46.8	1.42E-08	191.6	43.0	-1.16E-07	98.1	3.7	0.19	8.96E-08
Hbl1	RT	9 ±	6	1.31E-09	314.5	41.1	9.57E-11	91.6	40.0	-1.40E-09	202.6	23.1	0.10	1.11E-09
NMB535	RT	13 ±	3	4.55E-10	0.2	65.6	-5.09E-11	129.4	16.0	-4.05E-10	224.8	17.9	-0.18	3.53E-10